ACS central science

http://pubs.acs.org/journal/acscii

Research Article

Sensing Living Bacteria *in Vivo* Using D-Alanine-Derived ^{11}C Radiotracers

Matthew F. L. Parker, Justin M. Luu, Brailee Schulte, Tony L. Huynh, Megan N. Stewart, Renuka Sriram, Michelle A. Yu, Salma Jivan, Peter J. Turnbaugh, Robert R. Flavell, Oren S. Rosenberg,* Michael A. Ohliger,* and David M. Wilson*

Cite This: *ACS Cent. Sci.* 2020, 6, 155−165

Read Online

ACCESS | Metrics & More | Article Recommendations | Supporting Information

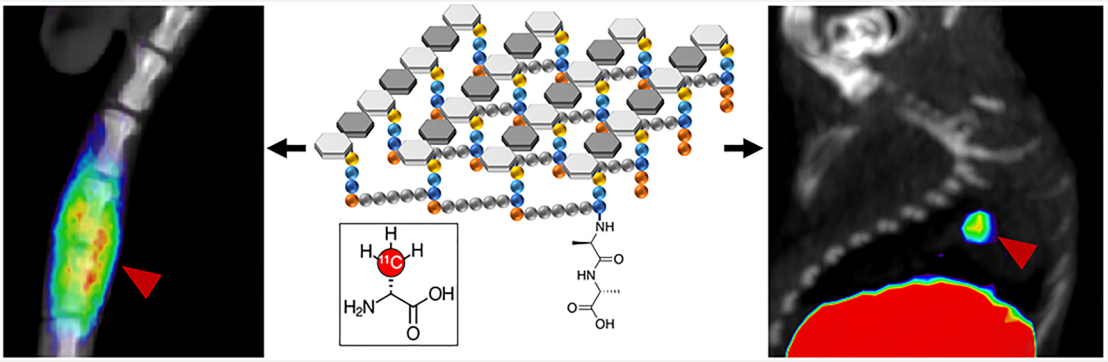

ABSTRACT: Incorporation of D-amino acids into peptidoglycan is a unique metabolic feature of bacteria. Since D-amino acids are not metabolic substrates in most mammalian tissues, this difference can be exploited to detect living bacteria *in vivo*. Given the prevalence of D-alanine in peptidoglycan muropeptides, as well as its role in several antibiotic mechanisms, we targeted this amino acid for positron emission tomography (PET) radiotracer development. D-[3-^{11}C]Alanine and the dipeptide D-[3-^{11}C]alanyl-D-alanine were synthesized via asymmetric alkylation of glycine-derived Schiff-base precursors with [^{11}C]methyl iodide in the presence of a cinchonidinium phase-transfer catalyst. In cell experiments, both tracers showed accumulation by a wide variety of both Gram-positive and Gram-negative pathogens including *Staphylococcus aureus* and *Pseudomonas aeruginosa*. In a mouse model of acute bacterial myositis, D-[3-^{11}C]alanine was accumulated by living microorganisms but was not taken up in areas of sterile inflammation. When compared to existing clinical nuclear imaging tools, specifically 2-deoxy-2-[^{18}F]fluoro-D-glucose and a gallium citrate radiotracer, D-alanine showed more bacteria-specific uptake. Decreased D-[3-^{11}C]alanine uptake was also observed in antibiotic-sensitive microbes after antimicrobial therapy, when compared to that in resistant organisms. Finally, prominent uptake of D-[3-^{11}C]alanine uptake was seen in rodent models of discitis-osteomyelitis and *P. aeruginosa* pneumonia. These data provide strong justification for clinical translation of D-[3-^{11}C]alanine to address a number of important human infections.

Many infection imaging approaches stem from established antimicrobial therapies, which target bacteria-specific structures to treat pathogens while minimizing damage to their human hosts. These structures include the bacterial isoforms of gyrase and topoisomerase IV, which are antagonized by fluoroquinolone antibiotics,[1] and the nascent peptide exit tunnel (NPET) of the bacterial ribosome, which is the target of macrocyclic lactones such as erythromycin.[2] Similarly, a common treatment for urinary tract infections is the Enterobacteriaceae-targeted pair of trimethoprim/sulfamethoxazole (TMP-SMX), which antagonize two steps of the folate biosynthesis pathway which is used by bacteria and not humans.[3] Examples of related diagnostic strategies include radiotracers developed for imaging bacteria via positron emission tomography (PET), namely, α-[^{11}C]PABA,[4] 2-[^{18}F]F-*p*-aminobenzoic acid,[5] and [^{18}F]fluoropropyl-trimethoprim.[6] These and other metabolism-targeted PET tracers represent elegant ways to detect living organisms *in vivo*.[7−10]

Both therapeutic and diagnostic strategies have also targeted bacterial peptidoglycan for microorganism-specific therapy and detection. The structure of peptidoglycan is shown in Figure 1, highlighting both the structural differences between Gram-negative and Gram-positive organisms and the D-alanine-derived component of bacterial muropeptides. Peptidoglycan is a strong and elastic polymer of the bacterial wall that maintains

Received: July 23, 2019
Published: February 4, 2020

https://dx.doi.org/10.1021/acscentsci.9b00743
ACS Cent. Sci. 2020, 6, 155−165

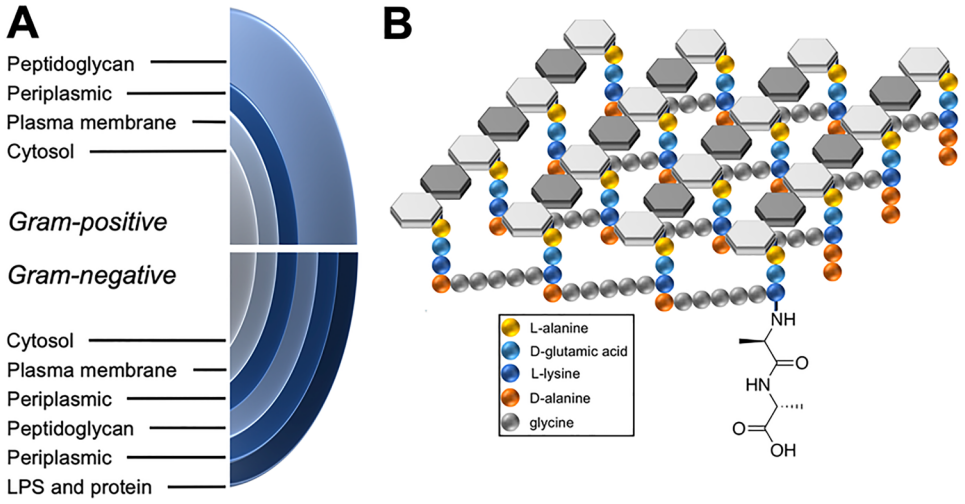

Figure 1. Structural features of bacterial peptidoglycan. (A) Structural differences in the bacterial cell wall between Gram-negative and Gram-positive organisms. Peptidoglycan constitutes 90% of Gram-positive organisms by dry weight. (B) Bacterial peptidoglycan highlighting cross-linking between muropeptides and the C-terminal D-ala–D-ala sequence.

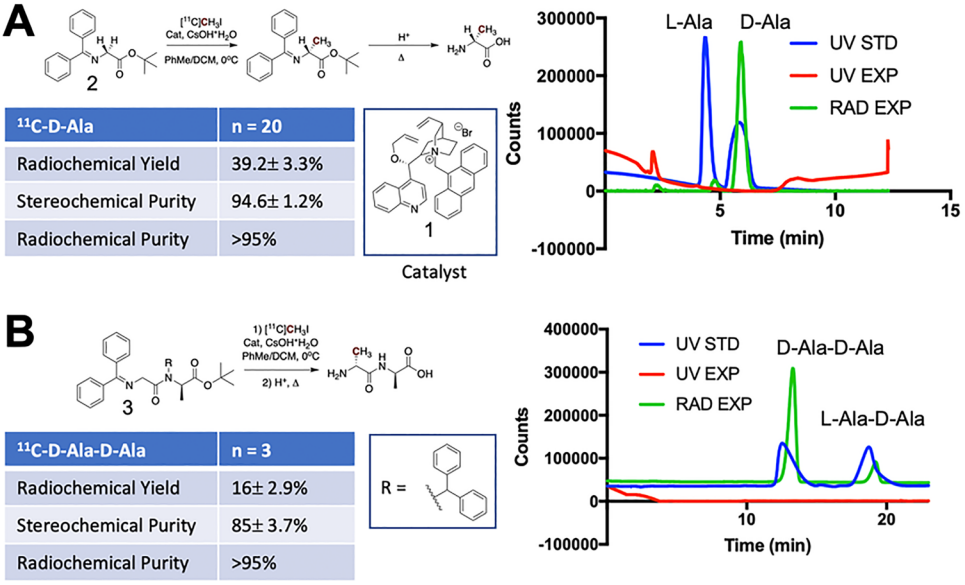

^{11}C-D-Ala	n = 20
Radiochemical Yield	39.2± 3.3%
Stereochemical Purity	94.6± 1.2%
Radiochemical Purity	>95%

^{11}C-D-Ala-D-Ala	n = 3
Radiochemical Yield	16± 2.9%
Stereochemical Purity	85± 3.7%
Radiochemical Purity	>95%

Figure 2. Radiochemical syntheses of D-[^{11}C]ala and D-[^{11}C]ala–D-ala using a chiral, phase-transfer cinchonidinium-derived catalyst. (A) High enantiomeric excess synthesis of D-[^{11}C]ala via asymmetric alkylation of a glycine-derived Schiff base with [^{11}C]CH_3I. The analytical HPLC data on the right shows the radioactive trace of D-[^{11}C]ala (green) overlaid with a racemic sample of alanine (blue) with both D- and L-enantiomers present in equal concentrations. (B) An analogous procedure was used for the radiosynthesis of D-[^{11}C]ala–D-ala at approximately 70% diastereomeric excess. The analytical HPLC data on the right show the radioactive trace of D-[^{11}C]ala–D-ala (green) overlaid with a sample containing D-ala–D-ala and the undesired diastereomer L-ala–D-ala present in equal concentrations (blue).

cell shape and anchors components of the cell envelope.[11] Interestingly, D-amino acids within peptidoglycan appear to protect the bacterial cell against peptidase and protease attacks and also serve important and specific roles in cell–cell signaling.[12] Many antimicrobial agents (both synthetic and natural products) work by antagonizing the D-alanine synthesis, dimerization, and integration pathway, most notably β-lactam antibiotics and other cell wall active agents like vancomycin[13] and cycloserine.[14] For detecting peptidoglycan, chemical strategies include direct labeling of the cell wall via fluorescent D-amino acids (DAAs), and identification of alkyne-bearing muropeptides via reporter probes.[15−17] We have recently labeled an amino acid D-[methyl-^{11}C]methionine (D-[^{11}C]met) for positron emission tomography (PET) imaging of infection, taking advantage of a known muropeptide retention mechanism.[18] This finding led us to consider other DAAs for PET, including canonical elements of peptidoglycan (D-alanine and D-glutamate) and other amino acids readily accumulated by bacteria *in vitro*, for example, D-phenylalanine and D-valine.[19]

For studying living bacteria *in vitro* and *in vivo*, one exciting radiopharmaceutical target would be a D-amino-acid-derived, PET radiotracer with high sensitivity to all or most species of bacteria. Numerous studies have demonstrated the muropeptide incorporation of exogenously administered D-amino acids including D-alanine, which represents a starting point for radiosynthesis of analogous ^{18}F or ^{11}C structures.[20−22] However, previous efforts have shown that ^{18}F-labeled derivatives of alanine are prone to defluorination *in vivo*,

https://dx.doi.org/10.1021/acscentsci.9b00743
ACS Cent. Sci. 2020, 6, 155−165

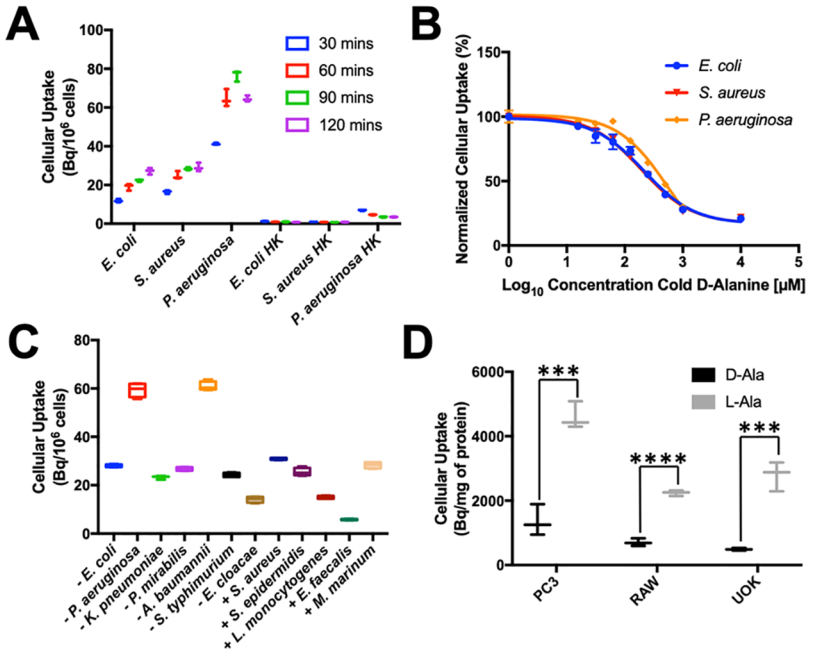

Figure 3. *In vitro* analysis of D-[^{11}C]ala in bacteria and mammalian cell lines. (A) Dynamic cellular uptake of D-[^{11}C]ala in *E. coli, S. aureus, and P. aeruginosa* in exponential-phase cultures at 30, 60, 90, and 120 min. No radioactivity was incorporated into heat-killed organisms. (B) Accumulation of D-[^{11}C]ala in the presence of increasing concentrations of unlabeled D-alanine. In both cases blocked uptake suggests specific incorporation. (C) Sensitivity analysis of D-[^{11}C]ala using a broad panel of human pathogens indicating avid uptake of tracer by nearly all organisms. (D) Comparison of D-[^{11}C]ala and L-[^{11}C]ala in mammalian cell lines. In all cases the accumulation of D-[^{11}C]ala was significantly lower, indicating its relative specificity for bacterial versus mammalian metabolism.

reflected in bone accumulation of radiolabel.[23] This instability would limit detection of bacteria-specific incorporation in bones or joint spaces, infections of which are a major clinical concern.[24,25] We therefore identified D-[3-^{11}C]alanine (D-[^{11}C]ala) and the dipeptide D-[3-^{11}C]alanyl-D-alanine (D-[^{11}C]ala–D-ala) as viable PET radiotracers, anticipated to be highly bacteria-avid given their structural homology to bacterial peptidoglycan precursors. These tracers were also designed to be sensitive to Gram-positive organisms including *Staphylococcus aureus* based on their rich peptidoglycan content.

Several strategies have been developed to synthesize endogenous ^{11}C amino acids for PET.[26] These include asymmetric alkylation of glycine-derived precursors using ^{11}C methyl iodide ([^{11}C]MeI) to generate L-[3-^{11}C]alanine. Reported precursors include [(+)-2-hydroxypinanyl-3-idene]-glycine *tert*-butyl ester (RCY, 12–28%; ee, 89%),[27] 2-*tert*-butyl-3-methyl-1,3-imidazolidin-4-one precursor (RCY, 75%; ee, 98%),[28] the Schiff base of (*S*)-*O*-[*N*-benzypropyl] amino] benzophenone-glycine-Ni complex (RCY, 60%; de, 60%),[29] (−)-8-phenylmethan-3-yl *N*-(diphenymethylene)glycinate precursor (RCY, 40%; ee, 52%),[30] and the camphor-derived Oppolzer's synthon (RCY, 40–50%; ee, 94%).[31] While these approaches were all considered feasible, we pursued [^{11}C]MeI alkylation of a glycine-derived Schiff base in the presence of a cinchonidinium phase-transfer catalyst[32−34] as a potential method to generate high enantiomeric excess D-[^{11}C]ala and D-[^{11}C]ala–D-ala.

In this work, we first synthesized these ^{11}C sensors, using a robust and enantioselective method, compatible with future human studies. We further demonstrated their sensitivity to a range of human pathogens *in vitro* in particular *S. aureus* and *Pseudomonas aeruginosa*. Finally, we showed bacteria-specific accumulation of D-[^{11}C]ala in several compelling preclinical models of acute bacterial infection.

RESULTS

Efficient, High-Stereochemical-Purity Radiosyntheses of D-[^{11}C]Ala and D-[^{11}C]Ala–D-ala. To target bacterial muropeptides, we developed stereoselective syntheses of D-[^{11}C]ala and D-[^{11}C]ala–D-ala that minimized generation of the undesired enantiomer and diastereomer, respectively. This was accomplished by adapting a recently published method using a phase-transfer cinchonidinium catalyst.[32−34] Asymmetric alkylation of glycine-derived precursors via [^{11}C]methyl iodide ([^{11}C]MeI), followed by acid-catalyzed hydrolysis of the carboxy and amino protecting groups, yielded D-[^{11}C]ala and D-[^{11}C]ala–D-ala in high enantiomeric excess (ee) and diastereomeric excess (de), respectively, as summarized in Figure 2. The solvent (toluene) and low temperature (0 °C) were essential for asymmetric induction. D-[^{11}C]Ala was obtained in 39.2% ± 3.3% (N = 20) decay-corrected radiochemical yield (RCY) with a radiochemical purity of >95% in all cases (D-[^{11}C]ala and the undesired L-[^{11}C]ala isomer together comprised >95% of the sample). Chiral HPLC analysis of the final product demonstrated a stereochemical purity of 94.6% ± 1.2% for the desired D-enantiomer (ee = 89.2%) (Figure 2A). Similarly, D-[^{11}C]ala–D-ala was also synthesized via a Schiff base precursor[35] and was obtained in 16% ± 2.9% (N = 3) decay-corrected RCY with a radiochemical purity of >95% in all cases. Chiral HPLC analysis of the final product demonstrated a stereochemical purity of 85% ± 3.7 (de = 70%) for the D,D-diastereomer (Figure 2B).

***In Vitro* Studies Using D-[^{11}C]Ala Showed Dramatic Tracer Accumulation in Most Human Pathogens, and**

https://dx.doi.org/10.1021/acscentsci.9b00743
ACS Cent. Sci. 2020, 6, 155−165

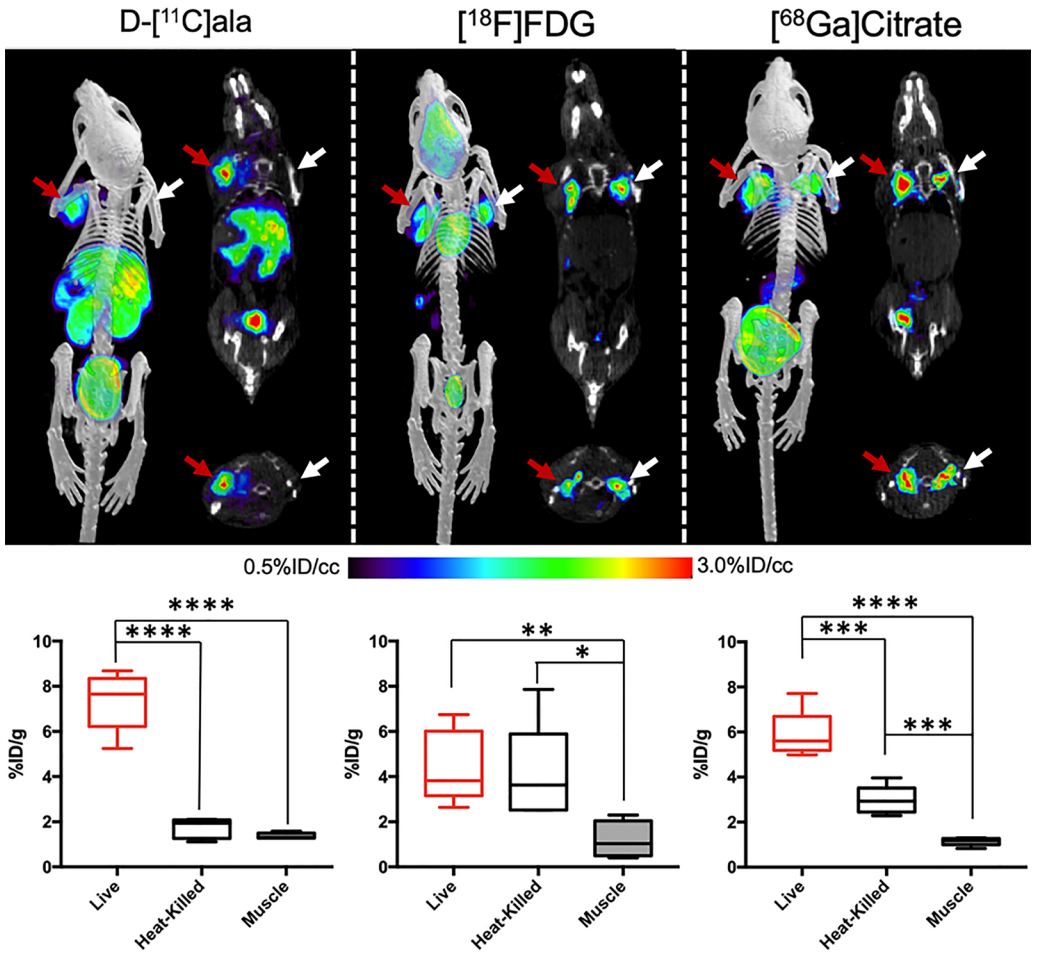

Figure 4. Performance of D-[^{11}C]ala in a murine model of acute bacterial infection. In all cases red arrows indicate the site of inoculation with live bacteria, while white arrows correspond to heat-killed bacteria. Representative images from μPET-CT studies using D-[^{11}C]ala, [^{18}F]FDG, and [^{68}Ga]gallium citrate are juxtaposed with the corresponding *ex vivo* tissue analyses. As reflected by the images, the mean D-[^{11}C]ala accumulation for tissues infected with live bacteria was 3.5-fold higher than that seen for heat-killed inoculation. In contrast, this difference was not seen for [^{18}F]FDG. For [^{68}Ga]gallium citrate a significant difference in tracer signal between inoculation sites was seen, but only 2-fold higher on the infected side.

Low Incorporation into Mammalian Cell Lines. To validate D-ala-derived radiotracers *in vitro*, we first applied D-[^{11}C]ala and D-[^{11}C]ala–D-ala to two representative human pathogens, namely, *E. coli* and *S. aureus*, Gram-negative and Gram-positive species, respectively. Based on these initial studies, D-[^{11}C]ala was chosen as our lead radiotracer, with *in vitro* data for D-[^{11}C]ala–D-ala presented in Figure S4. D-[^{11}C]Ala demonstrated increased incorporation over time when applied to small bacterial cultures (Figure 3A). Furthermore, D-[^{11}C]ala was not incorporated into heat-killed bacteria for all species studied. *E. coli*, *S. aureus*, and *P. aeruginosa* cultures were also incubated with D-[^{11}C]ala with increasing concentrations of unlabeled D-alanine (Figure 3B). D-[^{11}C]Ala uptake was outcompeted by cold D-alanine in all species with IC_{50} values of 216.1, 195.6, and 558.9 μM for *E. coli*, *S. aureus*, and *P. aeruginosa*, respectively. This similarity between competition assays despite the difference in quantity of peptidoglycan in Gram-negative and Gram-positive bacteria suggests that the saturation of uptake was not driven solely by substrate availability. We further investigated the sensitivity of D-[^{11}C]ala using a broader panel of clinically relevant pathogens. A radiotracer would be most useful in clinical practice if it could identify all or most bacteria, so that active infection could be differentiated from inflammation and other mimics. High incorporation of D-[^{11}C]ala was observed for nearly all of the species studied, including both Gram-negative and Gram-positive bacteria (Figure 3C). The sensitivities of D-[^{11}C]ala to all organisms were significantly higher than those seen with D-[^{11}C]met, with the two radiotracers compared in Figure S5. One somewhat surprising result was the incorporation of D-[^{11}C]ala into *P. aeruginosa*, an important hospital-acquired pathogen to which reported bacteria-specific detection strategies are largely insensitive.[36] This result motivated our subsequent studies in an animal model of *P. aeruginosa* infection, since diagnosis and treatment of this organism represent such significant challenges in cystic fibrosis and other patients.[37]

Finally, we investigated the specificity of D-alanine for bacterial versus mammalian metabolism by synthesizing L-[3-^{11}C]alanine (L-[^{11}C]ala) and incubating both alanine enantiomers with mammalian cells. Using identical conditions, L-[^{11}C]ala was synthesized via a commercially available cinchonidinium catalyst with an ee ~90%. *In vitro* analysis showed that both D-[^{11}C]ala and L-[^{11}C]ala were incorporated into bacteria (Figure S6), but the accumulation of D-[^{11}C]ala in mammalian cells was ~3–6-fold less than that observed for

https://dx.doi.org/10.1021/acscentsci.9b00743
ACS Cent. Sci. 2020, 6, 155–165

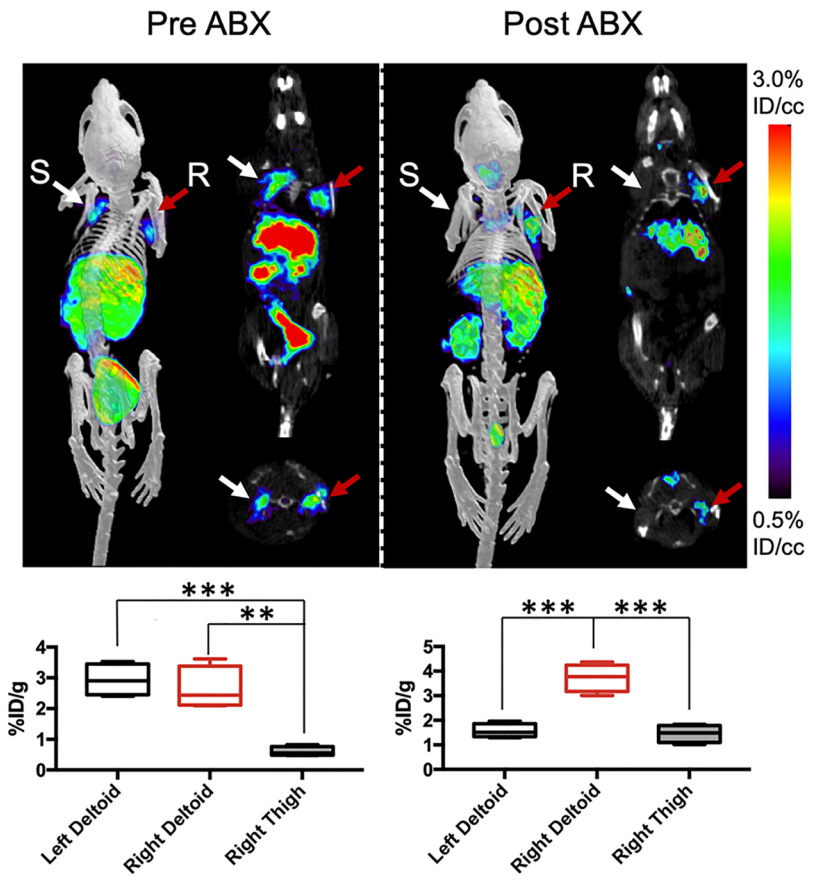

Figure 5. D-[^{11}C]Ala in a murine model of antimicrobial therapy. A cohort of mice were infected with both ampicillin-resistant bacteria (marked "R", red arrow) and ampicillin-sensitive bacteria (marked "S", white arrow). Since animals could not be sacrificed to obtain *ex vivo* data, the corresponding bar graphs indicate region-of-interest (ROI) analysis. The animals were imaged 5 h after inoculation with bilateral tracer activity seen, significantly higher than background muscle. After ampicillin administration and reimaging, there was no signal above background observed for the sensitive or "treated" bacteria, while persistent signal was seen corresponding to resistant organisms.

L-[^{11}C]ala (Figure 3D, P = 0.0009 to <0.0001). This result suggests specificity of D-[^{11}C]ala for living bacteria versus mammalian metabolism in both cancer (PC3, UOK) and inflammation (RAW 264.7).

***In Vivo* Analysis of D-[^{11}C]Ala in Conventionally Raised and Germ-Free Mice Showed Background Signal in Abdominal Organs, That Was Largely Independent of the Microbiome.** Before studying D-[^{11}C]ala in preclinical models of acute bacterial infection, the radiotracer was first applied to conventionally raised (CONV-R) and germ-free (GF) mice. These cohorts were used to evaluate the degree to which the uptake of D-[^{11}C]ala was dependent upon the microbiome. Animals were injected with 600 μCi of D-[^{11}C]ala, and sacrificed at approximately 90 min postinjection with organs studied for incorporated radioactivity via a γ counter. In CONV-R mice (N = 3), radiolabel was highest in the lungs, pancreas, kidneys, and liver with significant activity in the small and large bowel (Figure S7). This background activity likely reflects mammalian conversion of D-[^{11}C]ala, whose oxidation at the 2-position results in [3-^{11}C]pyruvate. Notably, the activity in bone and muscle was low (<2% ID/g), supporting our future application of this probe to imaging the musculoskeletal system. However, we did wish to determine what portion of D-[^{11}C]ala accumulation represented the microbiome, i.e., the complex communities of bacteria, archaea, microscopic eukaryotes, and viruses that inhabit the skin and aerodigestive tract of healthy animals. Therefore, D-[^{11}C]ala was also administered to a cohort of GF mice (N = 3) that were bred and raised in the absence of a microbiome. Identical workup of this cohort revealed that tracer signal in the two mouse populations was similar, except that a lower signal was seen in the large intestine of the GF cohort (Figure S7), P = 0.0138 for the large intestine and >0.05 in all other cases. This expected result indicates that, with the exception of uptake in the large intestine, the microbiome did not affect organ-specific activity.

D-[^{11}C]Ala Differentiated between Living Microorganisms and Sterile Inflammation in a Preclinical Model of Acute Bacterial Infection. One major goal of bacteria-specific radiotracers is to distinguish microbial growth from the host-dependent inflammatory response. A murine model of myositis was used to determine the specificity of D-[^{11}C]ala for living bacteria *in vivo*.[4−9,18] Mice were inoculated with 5 × 10^6 CFUs of live bacteria in the left shoulder musculature and with a 10-fold higher burden of heat-killed bacteria in the right shoulder musculature (N = 15 animals for *E. coli*, N = 10 animals for *S. aureus*). μPET/CT imaging using D-[^{11}C]ala demonstrated significant differences in the accumulation of the radiotracer into the site of live bacteria versus the site of heat-killed inoculation. These data were compared to those obtained using existing clinical nuclear imaging tools, namely, [^{18}F]fluoro−D-glucose ([^{18}F]FDG) and [^{68}Ga]gallium citrate in *S. aureus* (Figure 4) and *E. coli* (Figures S8−S10).

https://dx.doi.org/10.1021/acscentsci.9b00743
ACS Cent. Sci. 2020, 6, 155−165

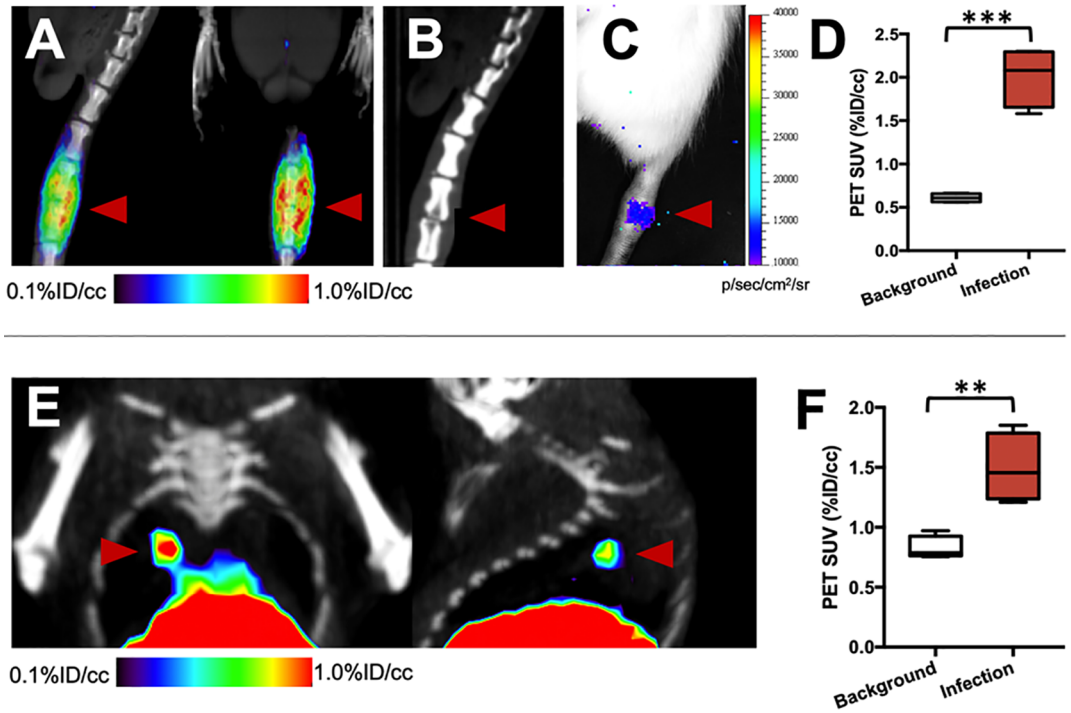

Figure 6. Imaging *S. aureus* vertebral discitis-osteomyelitis and *P. aeruginosa* pneumonia models using D-[^{11}C]ala. (A) Sagittal and coronal μPET-CT images from a study performed 4 days after inoculation, showing marked D-[^{11}C]ala accumulation at the spinal level inoculated with live *S. aureus*. (B) Computed tomography study performed at 10 days highlights the similarity between rodent and human discitis osteomyelitis. The red arrow highlights the affected level with disc-space narrowing and erosion of the adjacent end-plates. (C) Optical tomography image from the same rat, showing bioluminescent signal. (D) Region-of-interest analysis highlighting the difference between segments inoculated with live bacteria versus background (N = 4). (E) Coronal and sagittal images from a μPET-CT study using D-[^{11}C]ala in a murine *P. aeruginosa* model, generated via intratracheal inoculation of live bacteria. The red arrow corresponds to a focal pneumonia. (F) Region-of-interest analysis showing increased signal in infected lungs versus an uninfected cohort (N = 4).

Imaging findings were supported by *ex vivo* tissue analysis, for which a ∼3.5-fold difference is observed between the left and right shoulder musculature in *S. aureus*-infected animals (P = 0.0001). Studies using *E. coli*-infected animals showed a similar ∼3.3-fold difference between the two sides (P = 0.0001). Additionally, for both species there was no significant observed difference between muscle inoculated with heat-killed bacteria and background muscle, as observed in both the PET/CT imaging as well as *ex vivo* biodistribution (P = 0.1235 and 0.0974 for *S. aureus* and *E. coli*, respectively). By comparison, imaging using 2-deoxy-2-[^{18}F]fluoro−D-glucose ([^{18}F]FDG) (N = 10) showed similar uptake in both left and right shoulder muscles using PET/CT and via the *ex vivo* biodistribution analysis for both organisms (P > 0.05). This result has now been demonstrated in numerous studies for both *S. aureus* and *E. coli* infections using this model.[4−9,18] Since gallium-derived radiotracers are frequently used clinically in infected patients, [^{68}Ga]gallium citrate was also studied (N = 10). Using the same infection and imaging protocol, [^{68}Ga]gallium citrate accumulated in both the left and right shoulder musculature. However, only a ∼2-fold difference in uptake was measured from the *ex vivo* biodistribution analysis for *S. aureus* (P = 0.0008) and a ∼1.5-fold difference for *E. coli* (P = 0.0098).

Preclinical Models of Antibiotic Efficacy, Vertebral Discitis-Osteomyelitis, and *P. aeruginosa* Pneumonia Suggested That D-[^{11}C]Ala Could Be Used in Challenging Clinical Settings. Major diagnostic challenges using morphologic imaging techniques (computed tomography and magnetic resonance imaging) include demonstrating adequate antimicrobial therapy, distinguishing joint infection from other processes, and diagnosing acute pneumonia. We therefore studied the effects of antibiotic therapy on D-[^{11}C]ala accumulation and showed tracer uptake in a rat model of vertebral discitis-osteomyelitis (VDO) and in a mouse model of pneumonia.

We first developed a dual-infection myositis model whereby mice were simultaneously infected with both wild-type and resistant *E. coli* (2.5×10^6 CFUs each). Mice were inoculated with ampicillin-sensitive *E. coli* in the left shoulder and ampicillin-resistant bacteria in the right shoulder musculature to assess the ability of D-[^{11}C]ala to measure rapid response to antibiotic treatment. This cohort was studied using an image−treatment−image experimental protocol to which region-of-interest (ROI) analysis was applied (Figure 5). The pretreatment PET/CT images showed uptake into both left and right shoulders, without significantly different signals between the two sides (P = 0.5344). In contrast, the post-treatment PET/CT images showed a complete loss of signal in the left shoulder (site of antibiotic-susceptible *E. coli*), while the signal in the right shoulder was preserved (P = 0.0005).

To investigate the detection of pathogens in normally sterile joint spaces, a rat model of acute discitis-osteomyelitis was developed. In our clinical practice, discitis-osteomyelitis is seen in vulnerable patients with potentially dramatic neurologic consequences. We have previously found that the vast majority of discitis-osteomyelitis cases are caused by *S. aureus*, the organism to which D-[^{11}C]ala was targeted.[38] A cohort of rats (N = 4) were inoculated with 5×10^6 CFUs of bioluminescent *S. aureus* in the third intervertebral space from the base of the tail, and imaged on multiple days. Representative images from

https://dx.doi.org/10.1021/acscentsci.9b00743
ACS Cent. Sci. 2020, 6, 155−165

a rat are shown in Figure 6A−C. PET/CT imaging at day 4 showed dramatic radiotracer accumulation localized to the intervertebral injection site which is corroborated using bioluminescence imaging and was accompanied by bone erosion and joint-space narrowing at day 10 similar to abnormalities seen in patient studies. ROI analysis of PET signals at day 4 showed 3.3-fold excess signal at the infected level versus background tissue (P = 0.0002) (Figure 6D).

Finally, a preclinical model of *P. aeruginosa* infection was used to show that D-[^{11}C]ala could detect pneumonia-causing pathogens, even in a region of the body inhabited by commensal organisms. *P. aeruginosa* was chosen because detection of this organism represents such a profound challenge in clinical practice, in patients with cystic fibrosis in particular. In these patients, active pneumonia cannot be reliably differentiated from lung inflammation using any method. A cohort of mice (N = 5) were inoculated intratracheally with 2 × 10^6 CFUs of *P. aeruginosa* and imaged after approximately 6 h by PET. The results are shown in Figure 6E,F highlighting the detection of a focal pneumonia, with ROI analysis confirming higher radiotracer uptake in bacteria-infected lungs versus the lungs of normal mice (1.8-fold higher, P = 0.0046). This result was confirmed by *ex vivo* analysis (Figure S11).

DISCUSSION

Bacteria-specific metabolic pathways are compelling targets for imaging human infections. In this study, we developed an asymmetric synthesis of D-[^{11}C]ala and studied its performance in living systems. We observed exquisite sensitivity of D-[^{11}C]ala for nearly all human pathogens studied, and low radiotracer incorporation into mammalian cells. A biodistribution study in CONVR and GF mice showed that many normal organs incorporated the radiotracer, and that this incorporation was largely independent of commensal organisms. When applied to a murine infection model, PET using D-[^{11}C]ala showed the ability to distinguish living bacteria from sterile inflammation, more accurately than current imaging approaches such as [^{18}F]FDG or [^{68}Ga]gallium. This result suggests that the clinical use of both [^{18}F]FDG and gallium-derived radiotracers (predominantly [^{67}Ga]gallium) in infected patients[39−42] may over-report the presence of actively replicating bacteria. These data are also interesting given the variable mechanisms employed to generate image contrast. While [^{18}F]FDG is sensitive to the elevated glycolysis seen in activated immune cells, gallium-derived radiotracers are thought to work both by imaging the "acute phase" expression of the transferrin receptor, and siderophore-mediated uptake.[43] Therefore, ^{68}Ga may be acting as an iron(III) mimic and surrogate of bacterial iron metabolism.[44−46] In any case, PET imaging using [^{68}Ga]gallium citrate did show increased signal in tissue inoculated with living bacteria, versus tissue inoculated with heat-killed organisms. However, this difference was lower than that observed for D-[^{11}C]ala in the same model.

Additional experiments highlighted the clinical promise of D-[^{11}C]ala, which was applied to a dual infection model using antibiotic-sensitive and antibiotic-resistant organisms. The *in vivo* detection of antimicrobial resistance is a highly relevant unmet need in clinical medicine, with a sensitive imaging method needed to provide acutely ill patients with proper therapy. For this model, D-[^{11}C]ala could easily detect microorganism-specific killing. The specter of antibiotic resistance is addressed by D-[^{11}C]ala and related radiotracers in two ways: (1) high sensitivity to bacterial pathogens can indicate the presence of infection, versus a mimicking process, and (2) antibiotic response, or lack thereof, can be studied following empiric therapy. This diagnostic paradigm is particularly helpful since abnormalities seen on morphologic imaging (CT and MRI) frequently take days or weeks to resolve following administration of antibiotics.

The application of D-[^{11}C]ala to clinically challenging infections was also highlighted by imaging *S. aureus* in a rat model of acute spinal infection (VDO) and *P. aeruginosa* in a mouse model of acute pneumonia. VDO caused by *S. aureus* is an important clinical problem that highlights the need to sense Gram-positive organisms, in this case via peptidoglycan-targeted D-[^{11}C]ala being targeted. This disease is difficult to diagnose using conventional imaging methods, with acute infection and sterile inflammation appearing similar on CT and MRI exams. Similarly, pneumonia caused by *P. aeruginosa* is problematic especially in cystic fibrosis patients who are chronically colonized by this organism, and in whom dangerous infections cannot be reliably detected. Future application of D-[^{11}C]ala to patients with VDO and *P. aeruginosa* infection will be facilitated by the lack of D-alanine toxicity, obviating much of the preclinical testing required for the majority of ^{18}F tracers. The potential for translation of D-[^{11}C]ala is highlighted by our first-generation radiotracer, D-[^{11}C]met, which demonstrated broad organism sensitivity, low effective tissue doses, and lower barriers to institutional approval.[47]

One challenge for D-[^{11}C]ala (or any radiotracer) is interpreting imaging data in the context of background uptake. Nearly all PET tracers show background accumulation that limits the detection of disease in those locations—for example, [^{18}F]FDG cannot reliably detect abnormal metabolism in the brain due to extraordinary retention of ^{18}F by the cerebral cortex. In the case of probes targeting infection, the two issues are (1) metabolic clearance, i.e., probe metabolism in the liver, kidneys, and other organs, and (2) probe uptake by commensal bacteria in the skin and aerodigestive tract. Fortunately, many of the most clinically challenging infections are those that occur in normally sterile spaces such as joints. Our data presented for D-[3-^{11}C]alanine in a *P. aeruginosa* show that, even in organs and tissues such as the lungs, where there is some background, an infection can easily be detected. Furthermore, it is likely that chemical manipulation of the D-amino acid scaffold can be used to attenuate background signals related to mammalian metabolism. For example, C-terminal modifications and 2-position modifications (in particular deuteration) might be used to impede human oxidation of DAAs without changing peptidoglycan incorporation.[48,49]

An additional challenge with ^{11}C-derived radiotracers is their relatively short half-life ($t_{1/2}$ = 20 min). However, we believe that the rapid signal decay of D-[^{11}C]ala confers numerous advantages in the acute setting, for example, by allowing administration of two radiotracers in a single imaging period. Finally, the data obtained for this report strongly justify developing new ^{11}C or ^{18}F radiotracers homologous to D-[^{11}C]ala; the accumulation of this probe in bacteria (>50% of administered activity incorporated *in vitro* for several pathogens) is the highest we have observed for any tracer.

https://dx.doi.org/10.1021/acscentsci.9b00743
ACS Cent. Sci. 2020, 6, 155−165

METHODS

General Chemistry and Radiochemistry. Full descriptions of chemical and radiochemical syntheses, as well as the analytical techniques used, are provided in the Supporting Information. Unless otherwise noted, all reagents were obtained commercially and used without further purification. Radioisotopes were generated in the UCSF radiopharmaceutical facility.

General [^{11}C]Amino Acid and Dipeptide Synthesis. In a 5.5 mL borosilicate vial, the phase-transfer catalyst (1.5 mg, 2.4 μmol) and CsOH−H_2O (90 mg, 600 μmol) were suspended in a mixture of toluene/dichloromethane (400 μL, 9:1, v/v). The reaction vessel was cooled in an ice bath with rapid stirring, and [^{11}C]CH_3I and the Schiff-base precursor in 500 μL of toluene were added dropwise. The mixture was subsequently stirred for 15 min. After passing the reaction through a silica light sep pak (WAT023537) and subsequent elution with MeCN, 1 mL of TFA was added to the eluent with heating to 100 °C for 15 min. The reaction mixture was concentrated and diluted with MeCN × 3 to remove the TFA. The residue was dissolved in pH 7.4 PBS, and a sample was taken for analysis on a Phenomonex Chirex 3126 chiral column (1 mM $CuSO_4$).

***In Vitro* Bacterial Assays.** All studies using bacteria were supported by an approved institutional biological use authorization (BUA) protocol, and no unexpected or unusually high safety hazards were encountered. All bacterial strains were purchased from American Type Culture Collection (ATCC) except resistant *S. aureus* (Xen 29), which was purchased from PerkinElmer. Each strain was aerobically grown using conditions outlined in Figure S12. These cultures (4 mL) were pelleted by centrifugation at 8000*g* for 5 min and reconstituted in F12 media. Aliquots (625 μL) were added to 10 mL portions of F12 media. Radiotracer uptake assays were performed by incubating these bacterial subcultures with D-[^{11}C]ala or D-[^{11}C]ala−D-ala (370 kBq/mL) at 37 °C with rapid agitation. As a control, heat-killed (90 °C for 30 min) bacteria were similarly subcultured and incubated with the radiotracer. Bacteria (500 μL aliquots) were centrifuged 8000*g* for 5 min in a spin filter equipped with a 0.22 μm nylon filter. The filter cartridge was washed with PBS, and the activity for each pellet and filtrate was measured using an automated γ counter (Hidex). Four replicates were used for each assay. Counts for each sample were corrected for background and normalized to CFU or total protein. Protein estimation was performed using a Bradford assay.

μPET/CT Imaging. The same general protocol was used for all studies. A tail vein catheter was placed in mice under isoflurane anesthesia. For alanine studies, approximately 800 μCi of D-[^{11}C]ala was injected via the tail vein catheter. For gallium studies, approximately 200 μCi of [^{68}Ga]gallium citrate was injected via the tail vein catheter. For FDG studies, approximately 150 μCi of [^{18}F]FDG was injected via the tail vein catheter. The animals were placed on a heating pad to minimize shivering. Mice were allowed to recover and micturate, and at 45 min postinjection, placed back under isoflurane anesthesia. At 1 h postinjection, the animals were transferred to a Siemens Inveon micro PET-CT system (Siemens, Erlangen, Germany), and imaged using a single static 25 min PET acquisition followed by a 10 min micro-CT scan for attenuation correction and anatomical coregistration. No adverse events were observed during or after injection of any compound. Anesthesia was maintained during imaging using isofluorane. Upon completion of imaging, mice were sacrificed, and biodistribution analysis was performed. γ counting of harvested tissues was performed using a Hidex Automatic Gamma Counter (Turku, Finland).

Conventionally Raised (CONV-R) and Germ-Free (GF) Mice. All animal procedures were approved by the UCSF Institutional Animal Care and Use Committee, and all studies were performed in accordance with UCSF guidelines regarding animal housing, pain management, and euthanasia. Wild-type mice studied were CBA/J mice (female, 6−8 weeks old). Germ-free C67BL6/J mice were originally obtained from the National Gnotobiotic Rodent Resource Center and subsequently bred and maintained in the UCSF Gnotobiotic Core Facility under germ-free conditions, housed in flexible film isolators and fed Lab Diet 5021 breeder chow in accordance with the guidelines established by the Institutional Animal Care and Use Committee.

Murine Myositis Model. CBA/J mice (female, 6−8 weeks old) were used for all experiments. Mice were injected with different strains of live or 10× heat-killed (90 °C for 30 min) bacteria aerobically grown to absorbance of 1 at 600 nm in Lysogeny Broth (LB). Inoculations were performed by injection of 50 μL of bacteria into the shoulder musculature. The infections were allowed to develop for 10 h, and animals were subsequently injected with radiotracer and imaged.

Antibiotic Efficacy Studies. CBA/J mice (female, 6−8 weeks old) were used for all experiments. Mice were injected with different strains of live bacteria as above into the shoulder musculature. The infections were allowed to develop for 5 h. The mice were subsequently injected with D-[^{11}C]ala and imaged according to the same protocol. After the imaging was completed, the mice were treated with ampicillin (50 mg/kg) via the tail vein. After 3 h, the mice were again injected with D-[^{11}C]ala and imaged using the same protocol.

Vertebral Discitis-Osteomyelitis Model. Sprague/Dawley rats (male, 10−12 weeks old) were used for all experiments. The rats were injected with 50 μL of Xen 29 bioluminescent *S. aureus* aerobically grown to an absorbance of 1 at 600 nm in Lysogeny Broth (LB) with 100 μg/L of kanamycin. The rats were injected in the third intervertebral space from the base of the tail at 50% depth (based on the diameter of the tail) as described previously.[50] The infections were allowed to develop for 14 days. At different daily intervals, the rats were injected with a radiotracer and imaged according to the same protocol.

Pneumonia Lung Injection Model. CBA/J mice (female, 9−11 weeks old) were used for all experiments. The mice were injected with 50 μL of PA01 in PBS (aerobically grown to absorbance of 0.4 at 600 nm in Lysogeny Broth (LB)) intratracheally as described previously.[51] The infections were allowed to develop for 6 h. The mice were subsequently injected with D-[11C]ala and imaged according to the same protocol.

Data Analysis and Statistical Considerations. For synthesis, radiochemical yield incorporates decay-correction for ^{11}C ($t_{1/2}$ = 20 min). *In vitro* data were normalized to CFUs for sensitivity analysis to account for differential growth rates between organisms. All *in vivo* PET data were viewed using open source Amide software (amide.sourceforge.net). Quantification of uptake was performed by drawing spherical regions of interest (5−8 mm^3) over indicated organs on the CT portion of the exam, and expressed as percent injected dose per gram. All statistical analysis was performed using Microsoft

https://dx.doi.org/10.1021/acscentsci.9b00743
ACS Cent. Sci. 2020, 6, 155−165

Excel. Data were analyzed using an unpaired two-tailed Student's t test. All graphs are depicted with error bars corresponding to the standard error of the mean. Other data including specific activity, radiochemical yield, and % D-enantiomer are also reported as mean ± standard error.

■ ASSOCIATED CONTENT

Supporting Information

The Supporting Information is available free of charge at https://pubs.acs.org/doi/10.1021/acscentsci.9b00743.

Detailed information regarding synthesis, *in vitro*, and *in vivo* experiments not reported in the main text (PDF)

■ AUTHOR INFORMATION

Corresponding Authors

Oren S. Rosenberg − *Department of Medicine, University of California, San Francisco, San Francisco, California 94158, United States*; Phone: (415) 514-0412; Email: oren.rosenberg@ucsf.edu; Fax: (415) 476-9364

Michael A. Ohliger − *Department of Radiology and Biomedical Imaging, University of California, San Francisco, San Francisco, California 94158, United States; Department of Radiology, Zuckerberg San Francisco General Hospital, San Francisco, California 94110, United States*; Phone: (415) 206-8024; Email: michael.ohliger@ucsf.edu; Fax: (415) 206-4004

David M. Wilson − *Department of Radiology and Biomedical Imaging, University of California, San Francisco, San Francisco, California 94158, United States*; orcid.org/0000-0002-1095-046X; Phone: (415) 353-1668; Email: david.m.wilson@ucsf.edu; Fax: (415) 353-8593

Authors

Matthew F. L. Parker − *Department of Radiology and Biomedical Imaging, University of California, San Francisco, San Francisco, California 94158, United States*

Justin M. Luu − *Department of Radiology and Biomedical Imaging, University of California, San Francisco, San Francisco, California 94158, United States*

Brailee Schulte − *Department of Radiology and Biomedical Imaging, University of California, San Francisco, San Francisco, California 94158, United States*

Tony L. Huynh − *Department of Radiology and Biomedical Imaging, University of California, San Francisco, San Francisco, California 94158, United States*

Megan N. Stewart − *Department of Radiology and Biomedical Imaging, University of California, San Francisco, San Francisco, California 94158, United States*

Renuka Sriram − *Department of Radiology and Biomedical Imaging, University of California, San Francisco, San Francisco, California 94158, United States*; orcid.org/0000-0003-3505-2479

Michelle A. Yu − *Department of Medicine, University of California, San Francisco, San Francisco, California 94158, United States*

Salma Jivan − *Department of Radiology and Biomedical Imaging, University of California, San Francisco, San Francisco, California 94158, United States*

Peter J. Turnbaugh − *Department of Microbiology and Immunology, University of California, San Francisco, San Francisco, California 94158, United States*

Robert R. Flavell − *Department of Radiology and Biomedical Imaging, University of California, San Francisco, San Francisco, California 94158, United States*

Complete contact information is available at: https://pubs.acs.org/10.1021/acscentsci.9b00743

Author Contributions

D.M.W., M.A.O., and O.S.R. proposed and supervised the overall project. M.F.L.P., J.L., R.S. obtained *in vitro* data. M.F.L.P., M.N.S., B.S., and S.J. performed the radiochemistry. M.F.L.P., J.L., and T.L.H. performed μPET-CT imaging studies and subsequent data analysis. M.F.L.P. and D.M.W. performed *ex vivo* analysis. M.F.L.P., D.M.W., R.R.F., M.A.O., and O.S.R. wrote and edited the paper.

Funding

Grant sponsors NIH R01EB024014, NIH R01EB025985, R03AI138189, DOD A132172. UCSF Resource Allocation Program.

Notes

The authors declare no competing financial interest.

■ ACKNOWLEDGMENTS

The authors would like to thank Dr. Zack Brown for helpful discussion regarding precursor synthesis. The authors would like to thank the UCSF Gnotobiotic Core facility for providing animals. The authors would like to thank the UCSF Cyclotron Facility for production. The authors would like to thank Drs. Windhorst and Poot (Amsterdam VUMC) for their assistance with ^{11}C radiochemistry. The authors would like to also thank UCSF veterinarian Dr. Erin Katz for assistance and guidance with the animal models.

■ REFERENCES

(1) Aldred, K. J.; Kerns, R. J.; Osheroff, N. Mechanism of quinolone action and resistance. *Biochemistry* **2014**, *53* (10), 1565−1574.

(2) Vazquez-Laslop, N.; Mankin, A. S. How macrolide antibiotics work. *Trends Biochem. Sci.* **2018**, *43* (9), 668−684.

(3) Minato, Y.; Dawadi, S.; Kordus, S. L.; Sivanandam, A.; Aldrich, C. C.; Baughn, A. D. Mutual potentiation drives synergy between trimethoprim and sulfamethoxazole. *Nat. Commun.* **2018**, *9*, 1003.

(4) Mutch, C. A.; Ordonez, A. A.; Qin, H.; Parker, M.; Bambarger, L. E.; Villanueva-Meyer, J. E.; Blecha, J.; Carroll, V.; Taglang, C.; Flavell, R.; Sriram, R.; VanBrocklin, H.; Rosenberg, O.; Ohliger, M. A.; Jain, S. K.; Neumann, K. D.; Wilson, D. M. [^{11}C]Para-aminobenzoic acid: a positron emission tomography tracer targeting bacteria-specific metabolism. *ACS Infect. Dis.* **2018**, *4* (7), 1067−1072.

(5) Zhang, Z.; Ordonez, A. A.; Wang, H.; Li, Y.; Gogarty, K. R.; Weinstein, E. A.; Daryaee, F.; Merino, J.; Yoon, G. E.; Kalinda, A. S.; Mease, R. C.; Iuliano, J. N.; Smith-Jones, P. M.; Jain, S. K.; Tonge, P. J. Positron emission tomography imaging with 2-[^{18}F]F-p-amino-benzoic acid detects Staphylococcus aureus infections and monitors drug response. *ACS Infect. Dis.* **2018**, *4* (11), 1635−1644.

(6) Sellmyer, M. A.; Lee, I.; Hou, C.; Weng, C.; Li, S.; Lieberman, B. P.; Zeng, C.; Mankoff, D. A.; Mach, R. H. Bacterial infection imaging with [^{18}F]fluoropropyl-trimethoprim. *Proc. Natl. Acad. Sci. U. S. A.* **2017**, *114* (31), 8372−8377.

(7) Weinstein, E. A.; Ordonez, A. A.; DeMarco, V. P.; Murawski, A. M.; Pokkali, S.; MacDonald, E. M.; Klunk, M.; Mease, R. C.; Pomper, M. G.; Jain, S. K. Imaging Enterobacteriaceae infection in vivo with 18F-fluorodeoxysorbitol position emission tomography. *Sci. Transl. Med.* **2014**, *6*, 259.

(8) Ning, X.; Seo, W.; Lee, S.; Takemiya, K.; Rafi, M.; Feng, X.; Weiss, D.; Wang, X.; Williams, L.; Camp, V. M.; Eugene, M.; Taylor, W. R.; Goodman, M.; Murthy, N. PET imaging of bacterial infections

with fluorine-18-labeled maltohexaose. *Angew. Chem., Int. Ed.* **2014**, *53* (51), 14096−14101.
(9) Gowrishankar, G.; Hardy, J.; Wardak, M.; Namavari, M.; Reeves, R. E.; Neofytou, E.; Srinivasan, A.; Wu, J. C.; Contag, C. H.; Gambhir, S. S. Specific imaging of bacterial infection using 6″-18F-Fluoromaltotriose: a second-generation PET tracer targeting the maltodextrin transporter in bacteria. *J. Nucl. Med.* **2017**, *58* (10), 1679−1684.
(10) Auletta, S.; Varani, M.; Horvat, R.; Galli, F.; Signore, A.; Hess, S. PET radiopharmaceuticals for specific bacteria imaging: a systematic review. *J. Clin. Med.* **2019**, *8*, 197.
(11) Vollmer, W.; Blanot, D.; De Pedro, M. A. Peptidoglycan structure and architecture. *FEMS Microbiology Reviews.* **2008**, *32* (2), 149−167.
(12) Lam, H.; Oh, D. C.; Cava, F.; Takacs, C. N.; Clardy, J.; De Pedro, M. A.; Waldor, M. K. D-amino acids govern stationary phase cell wall remodeling in bacteria. *Science* **2009**, *325* (5947), 1552−1555.
(13) Hammes, W. P.; Neuhaus, F. C. On the mechanism of action of vancomycin: inhibition of peptidoglycan synthesis in Gaffkya homari. *Antimicrob. Agents Chemother.* **1974**, *6* (6), 722−728.
(14) Lambert, M. P.; Neuhaus, F. C. Mechanism of D-cycloserine action: alanine racemase from Escherichia coli W. *J. Bacteriol.* **1972**, *110* (3), 978−987.
(15) Hsu, Y.; Rittichier, J.; Kuru, E.; Yablonowski, J.; Pasciak, E.; Tekkam, S.; Hall, E.; Murphy, B.; Lee, T. K.; Garner, E. C.; Huang, K. C.; Brun, Y. V.; VanNieuwenhze, M. S. Full color palette of fluorescent D-amino acids for *in situ* labeling of bacteria cell walls. *Chem. Sci.* **2017**, *8* (9), 6313−6321.
(16) Pidgeon, S. E.; Fura, J. M.; Birabaharan, M.; Vezenov, D.; Pires, M. M. Metabolic profiling of bacteria by unnatural C-terminated D-amino acids. *Angew. Chem., Int. Ed.* **2015**, *54* (21), 6158−6162.
(17) Siegrist, M. S.; Whiteside, S.; Jewett, J. C.; Aditham, A.; Cava, F.; Bertozzi, C. R. D)-amino acid chemical reporters reveal peptidoglycan dynamics of an intracellular pathogen. *ACS Chem. Biol.* **2013**, *8* (3), 500−505.
(18) Neumann, K. D.; Villanueva-Meyer, J. E.; Mutch, C. A.; Flavell, R. R.; Blecha, J. E.; Kwak, T.; Sriram, R.; VanBrocklin, H. F.; Rosenberg, O. S.; Ohliger, M. A.; Wilson, D. M. Imaging active infection in vivo using D-amino acid derived PET radiotracers. *Sci. Rep.* **2017**, *7*, 7903.
(19) Caparros, M.; Pisabarro, A. G.; De Pedro, M. A. Effect of D-amino acids on structure and synthesis of peptidoglycan in Escherichia coli. *J. Bacteriol.* **1992**, *174* (17), 5549−5559.
(20) Wargel, R. J.; Shadur, C. A.; Neuhaus, F. C. Mechanism of D-cycloserine action: transport systems for D-alanine, D-cycloserine, L-alanine, and glycine. *J. Bacteriol.* **1970**, *103* (3), 778−788.
(21) Robbins, J. C.; Oxender, D. L. Transport systems for alanine, serine, and glycine in Escherichia coli K-12. *J. Bacteriol.* **1973**, *116* (1), 12−18.
(22) Izaki, K.; Matsuhashi, M.; Strominger, J. L. Biosynthesis of the peptidoglycan of bacterial cell walls. 8. Peptidoglycan transpeptidase and D-alanine carboxypeptidase: penicillin-sensitive enzymatic reaction in strains of Escherichia coli. *J. Biol. Chem.* **1968**, *243* (11), 3180−3192.
(23) Wang, L.; Zha, Z.; Qu, W.; Qiao, H.; Lieberman, B. P.; Plössl, K.; Kung, H. F. Synthesis and evaluation of ^{18}F labeled alanine derivatives as potential tumor imaging agents. *Nucl. Med. Biol.* **2012**, *39* (7), 933−943.
(24) Talbott, J. F.; Shah, V. N.; Uzelac, A.; Narvid, J.; Dumont, R. A.; Chin, C. T.; Wilson, D. M. Imaging-based approach to extradural infections of the spine. *Semin. Ultrasound CT MR.* **2018**, *39* (6), 570−586.
(25) Tande, A. J.; Patel, R. Prosthetic joint infection. *Clin. Microbiol. Rev.* **2014**, *27* (2), 302−345.
(26) Pekošak, A.; Filp, U.; Poot, A. J.; Windhorst, A. D. From carbon-11-labeled amino acids to peptides in positron emission tomography: the synthesis and clinical applications. *Mol. Imaging Biol.* **2018**, *20*, 510−532.
(27) Antoni, G.; Langstrom, B. Asymmetric synthesis of L-[3−11C]alanine. *Acta Chem. Scand.* **1986**, *40*, 152−156.
(28) Fasth, K. J.; Hornfeldt, K.; Langstrom, B. Asymmetric synthesis of 11C-labelled L and D amino acids by alkylation of imidazolidinone derivates. *Acta Chem. Scand.* **1995**, *49*, 301−304.
(29) Fasth, K.; Långström, B. Asymmetric synthesis of L-[beta-11C]amino acids using a chiral nickel complex of the Schiff Base of (S)-o-[(N-benzylprolyl)amino]benzophenone and glycine. *Acta Chem. Scand.* **1990**, *44*, 720−725.
(30) Fasth, K.; Antoni, G.; Langstrom, B. Asymmetric synthesis of L-[3−11C]alanine and L-[11C]phenylalanin by a phase-transfer alkylation reaction. *J. Chem. Soc., Perkin Trans. 1* **1988**, *12*, 3081−3084.
(31) Någren, K. Asymmetric synthesis of L-[3−11C]alanine utilizing a sultam derived glycine equivalent. Proceedings of the XIIth International Symposium 2136 Current Organic Chemistry, 2013, Vol. 17, No. 19 Popkov and Elsinga on Radiopharmaceutical Chemistry, Uppsala, Sweden, June 15 - 19, 1997. *J. Labelled Compd. Radiopharm.* **1997**, *40*, 758−759.
(32) Filp, U.; Pekošak, A.; Poot, A. J.; Windhorst, A. D. Enantioselective synthesis of carbon-11 labeled L- alanine using phase transfer catalysis of Schiff bases. *Tetrahedron* **2016**, *72*, 6551−6557.
(33) Pekošak, A.; Rotstein, B. H.; Collier, T. L.; Windhorst, A. D.; Vasdev, N.; Poot, A. J. Stereoselective ^{11}C labeling of a "native" tetrapeptide by using asymmetric phase-transfer catalyzed alkylation reactions. *Eur. J. Org. Chem.* **2017**, *5*, 1019−1024.
(34) Filp, U.; Pekošak, A.; Poot, A. J.; Windhorst, A. D. Sterocontrolled [^{11}C]alkylation of N-terminal glycine Schiff bases to obtain dipeptides. *Eur. J. Org. Chem.* **2017**, *37*, 5592−5596.
(35) Brown, Z. Z.; Scafmeister, C. E. Exploiting an inherent neighboring group effect of alpha-amino acids to synthesize extremely hindered dipeptides. *J. Am. Chem. Soc.* **2008**, *130* (44), 14382−14383.
(36) Ordonez, A. A.; Weinstein, E. A.; Bambarger, L. E.; Saini, V.; Chang, Y. S.; DeMarco, V. P.; Klunk, M. H.; Urbanowski, M. E.; Moulton, K. L.; Murawski, A. M.; Pokkali, S.; Kalinda, A. S.; Jain, S. K. A systematic approach for developing bacteria-specific imaging tracers. *J. Nucl. Med.* **2017**, *58* (1), 144−150.
(37) Ratjen, F.; Bell, S. C.; Rowe, S. M.; Goss, C. H.; Quittner, A. L.; Bush, A. Cyctic firbrosis. *Nat. Rev. Dis. Primers.* **2015**, *1*, 15010.
(38) Dumont, R. A.; Keen, N. N.; Bloomer, C. W.; Schwartz, B. S.; Talbott, J.; Clark, A. J.; Wilson, D. M.; Chin, C. T. Clinical utitily of diffusion-weighted imaging in spinal infections. *Clinical Neuroradiology.* **2019**, *29* (3), 515−522.
(39) Vorster, M.; Maes, A.; Wiele, C. V.; Sathekge, M. Gallium-68 PET: a powerful generator-based alternative to infection and inflammation imaging. *Semin. Nucl. Med.* **2016**, *46* (5), 436−437.
(40) Segard, T.; Morandeau, L. M.; Dunne, M. L.; Robinson, J. O.; Murray, R. J.; Geelhoed, E. A.; Francis, R. J. Comparison between Gallium-68 citrate PET-CT and Gallium-67 citrate scintigraphy for infection imaging. *Intern. Med. J.* **2019**, *49*, 1016.
(41) Salomaki, S. P.; Kemppainen, J.; Hohenthal, U.; Luoto, P.; Eskola, O.; Nuutila, P.; Seppanen, M.; Pirila, L.; Oksi, J.; Roivainen, A. Head-to-head comparison of ^{68}Ga-citrate and ^{18}F-FDG PET/CT for detection of infectious foci in patients with *Staphylococcus aureus* bacteraemia. *Contrast Media Mol. Imaging* **2017**, *2017*, 3179607.
(42) Smids, C.; Kouijzer, I. J.; Vos, F. J.; Sprong, T.; Hosman, A. J.; de Rooy, J. W.; Aarntzen, E. H.; de Geus-Oei, L. F.; Oyen, W. J.; Bleeker-Rovers, C. P. A comparison of the diagnostic value of MRI and ^{18}F-FDG-PET/CT in suspected spondylodiscitis. *Infection* **2017**, *45* (1), 41−49.
(43) Hoffer, P. Gallium: mechanisms. *J. Nucl. Med.* **1980**, *21* (3), 282−285.
(44) Petrik, M.; Uniaufova, E.; Raclavsky, V.; Palyzova, A.; Havlicek, V.; Haas, H.; Novy, Z.; Dolezal, D.; Hajduch, M.; Decristoforo, C. Imaging of *Pseudomonas aeruginosa* infection with Ga-68 labelled pyoverdine for positron emission tomography. *Sci. Rep.* **2018**, *8* (1), 15698.

https://dx.doi.org/10.1021/acscentsci.9b00743
ACS Cent. Sci. 2020, 6, 155−165

(45) Ioppolo, J. A.; Caldwell, D.; Beiraghi, O.; Llano, L.; Blacker, M.; Valliant, J. F.; Berti, P. J. 67Ga-labeled deferoxamine derivatives for imaging bacterial infection: preparation and screening of functionalized siderophore complexes. *Nucl. Med. Biol.* **2017**, *52*, 32−41.
(46) Petrik, M.; Zhai, C.; Haas, H.; Decristoforo, C. Siderophores for molecular imaging applications. *Clin. Transl. Imaging.* **2017**, *5* (1), 15−27.
(47) Stewart, M. N.; Parker, M. F. L.; Jivan, S.; Luu, J. M.; Huynh, T. L.; Schulte, B.; Seo, Y.; Blecha, J. E.; Villanueva-Meyer, J. E.; Flavell, R. R.; VanBrocklin, H. F.; Ohliger, M. A.; Rosenberg, O.; Wilson, D. M. High enantiomeric excess in-loop synthesis of D-[methyl-^{11}C]-methionine for use as a diagnostic positron emission tomography radiotracer in bacterial infection. *ACS Infect. Dis.* **2019**, *6* (1), 43−49.
(48) Pidgeon, S. E.; Fura, J. M.; Leon, W.; Birabaharan, M.; Vezenov, D.; Pires, M. M. Metabolic profiling of bacteria by unnatural C-terminated D-amino acids. *Angew. Chem., Int. Ed.* **2015**, *54*, 6158−6162.
(49) Molla, G. Competitive inhibitors unveil structure/function relationships in human D-amino acid oxidase. *Front. Mol. Biosci.* **2017**, *4*, 80.
(50) Bostian, P. A.; Karnes, J. M.; Cui, S.; Robinson, L. J.; Daffner, S. D.; Witt, M. R.; Emery, S. E. Novel rat tail discitis model using bioluminescent *Staphylococcus aureus*. *J. Orthop. Res.* **2017**, *35* (9), 2075−2081.
(51) Su, X.; Looney, M.; Robiquet, L.; Fang, X.; Matthay, M. A. Direct visual instillation as a method for efficient delivery of fluid into the distal airspaces of anesthetized mice. *Exp. Lung Res.* **2004**, *30* (6), 479−493.

https://dx.doi.org/10.1021/acscentsci.9b00743
ACS Cent. Sci. 2020, 6, 155−165